SPIN STRUCTURE MEASUREMENTS FROM E155 AT SLAC

Lee Sorrell*
American University
SLAC, MS 44
Stanford University, Stanford, CA 94309

Representing the E155 Collaboration

ABSTRACT

The E155 collaboration at SLAC has collected precise polarized deep inelastic scattering data which will provide further insights into the structure of the nucleon. The SLAC 48.3 GeV electron beam was used to obtain data from both proton and deuteron targets covering $0.01 < x < 0.9$ and $1(\mathrm{GeV/c})^2 < Q^2 < 40(\mathrm{GeV/c})^2$. E155 is the first high dose electron scattering experiment to use lithium deuteride (^{6}Li^{2}H) as a target material.

*Supported by DOE Contract DE–AC03–76F00515.

© 1998 by Lee Sorrell.

1 Introduction

Polarized deep inelastic scattering is a powerful tool for studying the internal spin structure of the proton and neutron (collectively known as nucleons).[1] Early results obtained by experiments at SLAC[2,3] and CERN[4] indicated the quarks contribute very little to the nucleon's spin. This contridicted expectations based on the naive quark-parton model (QPM), in which one expects the valence quarks to carry the nucleon spin, and led to the "spin crisis". This motivated additional theoretical and experimental studies of the spin structure of the nucleon which have yielded a richer view of the nucleon. Experiments at CERN,[5] SLAC,[6–9] and DESY[10] have provided increasing levels of precision and enabled the determination of polarized parton distribution functions (PDFs) using next-to-leading-order perturbative QCD calculations and the (Altarelli-Parisi or DGLAP) evolution equations such as the fits performed by E154[8] and SMC.[11] The main goal of the E155 experiment was to obtain large samples for both the proton and deuteron covering the widest possible kinematic range in a single experiment in order to constrain the polarized PDFs.

1.1 Inclusive Deep Inelastic Scattering

The SLAC experiments have focussed on inclusive deep inelastic scattering, in which only the scattered electron is detected (see Fig. 1). The kinematics of the scattering event are determined by the incident electron energy (E) and the energy (E′) and angle (θ) of the scattered electron with respect to the incident beam direction. From this information we can determine the 4-momentum transfer squared Q^2, and the Bjorken scaling variable $x = \frac{Q^2}{2M\nu} = \frac{Q^2}{2M(E-E')}$. The Bjorken scaling variable gives the fraction of the nucleon momentum carried by the struck quark.

In the unpolarized case, the cross section obtained from the inclusive measurements can be related to the unpolarized structure functions F_1 and F_2 as shown in Eq. 1.

$$\frac{d\sigma}{d\Omega dE'} = \frac{4\alpha^2 E'^2 cos^2(\theta/2)}{Q^4}\left[\frac{F_2(x,Q^2)}{\nu} + \frac{2F_1(x,Q^2)}{M}\tan^2(\theta/2)\right] \quad (1)$$

In this equation, M is the nucleon mass and θ is the scattering angle with respect to the original beam direction. In leading order, the structure function F_1 is given by a sum over the spin-averaged parton distributions

$$F_1(x,Q^2) = \frac{1}{2}\sum_i e_i^2[q_i^{\uparrow}(x,Q^2) + q_i^{\downarrow}(x,Q^2)]. \quad (2)$$

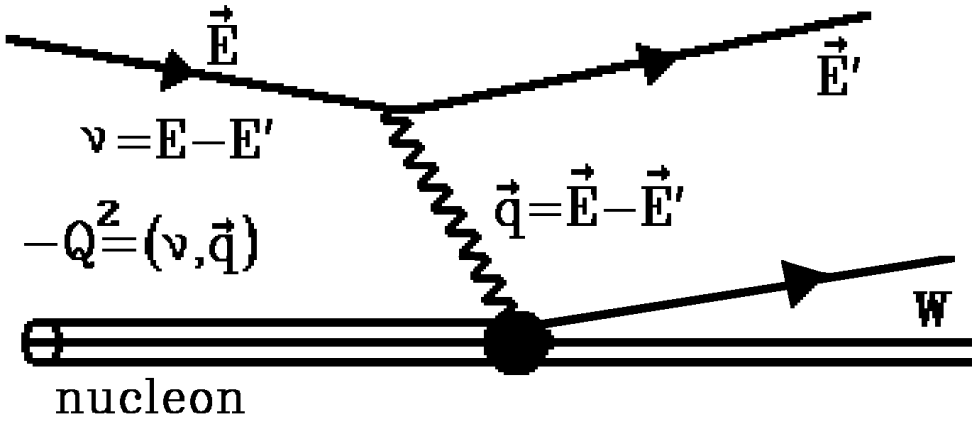

Fig. 1. Inclusive deep inelastic scattering.

The functions $q_i^{\uparrow}(x, Q^2)$ and $q_i^{\downarrow}(x, Q^2)$ are the probability distributions for the ith quark flavor to be aligned and anti-aligned with the nucleon spin (respectively). The index i in the sum runs over the kinematically allowed quark flavors and e_i is the corresponding charge.

1.2 Virtual Photon-Nucleon Asymmetries

In the polarized case, cross section asymmetries are measured and the polarized structure functions g_1 and g_2 are determined from these asymmetries. A simple way to understand how these asymmetries provide information on the net quark polarization is to first consider the case of a polarized virtual photon incident on a polarized nucleon. If the nucleon is polarized along the direction of the photon motion, then we can measure the longitudinal virtual photon asymmetry

$$A_1(x, Q^2) = \frac{\sigma_T^{1/2} - \sigma_T^{3/2}}{\sigma_T^{1/2} + \sigma_T^{3/2}} = \frac{g_1(x, Q^2) - \gamma^2 g_2(x, Q^2)}{F_1(x, Q^2)} \tag{3}$$

in which $\gamma^2 = Q^2/\nu^2$. The transverse virtual photoabsorption cross sections $\sigma_T^{1/2}$ and $\sigma_T^{3/2}$ are measured with the virtual photon polarization anti-aligned and aligned with the nucleon spin. In leading order, a spin-1 virtual photon with its spin aligned with the nucleon will couple to the quarks with spins anti-aligned with the nucelon spin and flip them from $s_z = -1/2$ to $+1/2$ (where s_z indicates the spin component along the beam axis). Similarly a photon with its spin anti-aligned with the nucleon spin will couple with the quarks that have their spins aligned with the nucleon spin. In this naive picture we will have $\sigma_T^{1/2} \sim \frac{1}{2} \sum_i e_i^2 q_i^{\uparrow}$ and $\sigma_T^{3/2} \sim \frac{1}{2} \sum_i e_i^2 q_i^{\downarrow}$.

The other virtual photon asymmetry A_2 is related to the transverse-longitudinal interference term σ_{LT}

$$A_2(x,Q^2) = \frac{2\sigma_{TL}}{\sigma_T^{1/2} + \sigma_T^{3/2}} = \gamma \frac{g_1(x,Q^2) + g_2(x,Q^2)}{F_1(x,Q^2)}. \tag{4}$$

This asymmetry does not lend itself to the naive interpretations given above, but does play a role in the extraction of the structure functions. In the past, $A_2 = 0$ has been used in the determination of the structure functions, but more recent data suggest that while A_2 is small, it is not consistent with zero.

1.3 Polarized DIS

At SLAC, cross section asymmetries are measured using polarized electrons, which interact with the polarized nucleons through the exchange of virtual photons (see Fig. 2). The "depolarization" factor, which reflects the difference between the electron polarization and virtual photon polarization, can be calculated and used in relating the experimental asymmetries to the desired structure functions. The cross section asymmetry $A_\parallel$ is obtained by polarizing the target parallel to the direction of the beam and measuring the difference in scattering rates for left and right electron helicity

$$A_\parallel = \frac{\sigma^{\downarrow\uparrow} - \sigma^{\uparrow\uparrow}}{\sigma^{\downarrow\uparrow} + \sigma^{\uparrow\uparrow}} = f_k \left\{ g_1(x,Q^2)[E + E'\cos\theta] - \frac{Q^2}{\nu} g_2(x,Q^2) \right\}. \tag{5}$$

The factor f_k includes the unpolarized structure function F_1 and the ratio of the transverse and longitudinal virtual photon cross sections R

$$f_k = \frac{1-\epsilon}{\nu F_1(x,Q^2)[1 + \epsilon R(x,Q^2)]} \tag{6}$$

where

$$\epsilon = \left[1 + 2(1 + \frac{\nu^2}{Q^2}) \tan^2(\theta/2) \right]^{-1}. \tag{7}$$

In the expression for the cross section asymmetry, the first arrow indicates the electron helicity and the second arrow indicates the target helicity. The SLAC experiments have also performed the same measurement with the target polarization reversed to minimize electroweak contributions and check for systematic effects. This experimental asymmetry can be related to the virtual photon asymmetries using

$$A_\parallel = D(A_1 + \eta A_2) \tag{8}$$

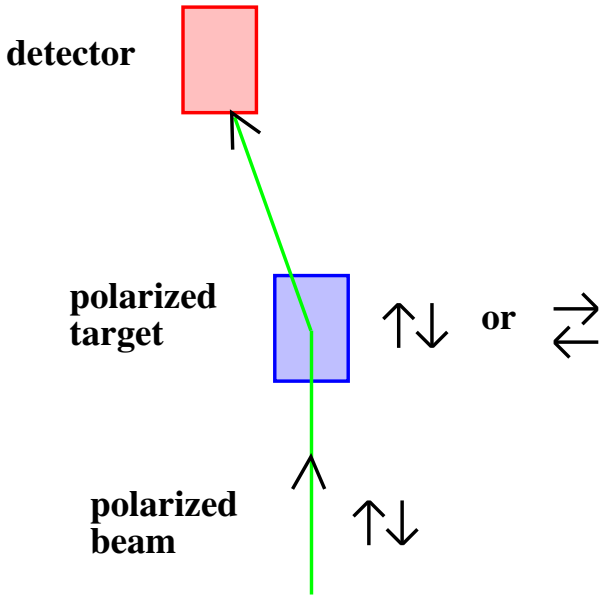

Fig. 2. Polarized inclusive deep inelastic scattering.

where $\eta = \epsilon\sqrt{Q^2}/(E - E'\epsilon)$ and the depolarization factor is given by $D = (1 - E'\epsilon/E)/(1 + \epsilon R)$. Since A_2 is typically small, we see that $A_{\|} \approx DA_1$, i.e. the asymmetry obtained using electrons is proportional to the virtual photon asymmetry, but is reduced by the depolarization factor.

Another experimental cross section asymmetry $A_\perp$ is obtained by polarizing the target in a direction transverse to the beam and measuring the rates for incident electrons with left and right helicity

$$A_\perp = \frac{\sigma^{\downarrow\leftarrow} - \sigma^{\uparrow\leftarrow}}{\sigma^{\downarrow\leftarrow} + \sigma^{\uparrow\leftarrow}} = f_k E' \sin\theta \left\{ g_1(x,Q^2) + \frac{2E}{\nu} g_2(x,Q^2) \right\}. \tag{9}$$

As in Eq. 5, the factor f_k is given by Eq. 6. For the recent SLAC experiments, θ is small, so $A_\perp$ is primarily sensitive to g_2, whereas $A_{\|}$ is primarily sensitive to g_1.

1.4 Polarized structure functions

Using Eqs. 2 and 3, one can see that in leading order we expect the longitudinal structure function g_1 to be given by

$$g_1(x,Q^2) = \frac{1}{2}\sum_i e_i^2 \Delta q_i = \frac{1}{2}\sum_i e_i^2 [q_i^{\uparrow}(x,Q^2) - q_i^{\downarrow}(x,Q^2)] \tag{10}$$

where Δq_i is the polarized quark distribution for the ith quark flavor. In leading order, g_1 is only sensitive to the net quark polarizations. In particular, the data from the

isoscalar deuteron target provides a particularly strong constraint on the net quark polarization $\Delta\Sigma = \Delta u + \Delta d + \Delta s$. However, in next-to-leading order (NLO) perturbative QCD (PQCD) g_1 is also sensitive to the polarized gluon distribution ΔG through the Q^2 evolution of the parton distributions and we can use the factorization theorem[12,13] to express g_1 as

$$g_1(x,Q^2) = \frac{1}{2}\sum_q e_q^2 \left[C_q \bigotimes \Delta q + \frac{1}{N_f} C_G \bigotimes \Delta G \right] \tag{11}$$

In this equation, N_f is the number of accessible quark flavors and the sum runs over the quark and anti-quark flavors. The coefficients C_q and C_g are the Wilson coefficients and correspond to the photon-quark and photon-gluon hard scattering cross sections. The convolution $\bigotimes$ is given by

$$(C \bigotimes q)(x,Q^2) = \int_x^1 \frac{dz}{z} C\left(\frac{x}{z}, \alpha_s\right) q(z,Q^2) \tag{12}$$

where $\alpha_s(Q^2)$ is the running coupling for the strong interaction. The Q^2 evolution of the parton distributions is governed by the Altarelli-Parisi (or DGLAP) evolution equations.[14] This evolution reflects the increasing resolution of our "microscope" as we increase Q^2. One important consequence of this evolution is to link the quark distributions to the gluon distributions through g $\rightarrow$ gq splitting. This makes it possible to indirectly measure the gluon distributions by measuring the quark distributions over a wide range in Q^2. Given sufficient statistical power over a wide range in x and Q^2, an NLO PQCD analysis of the Q^2 dependence of g_1 can be used to constrain the net polarization of the gluon.

Although the naive picture of the g_2 structure function is somewhat unclear, twist-2 calculations from Wandzura and Wilczek provide a relation between g_2 to g_1 via[15]

$$g_2(x,Q^2) = -g_1(x,Q^2) + \int_x^1 g_1(\xi,Q^2) d\xi/\xi \tag{13}$$

More generally, we expect

$$g_2(x,Q^2) = g_2^{WW}(x,Q^2) - \int_x^1 \frac{\partial}{\partial y}\left(\frac{m}{M} h_T(y,Q^2) + \xi(y,Q^2)\right)\frac{dy}{y} \tag{14}$$

where the second and third terms are twist-2 and -3 (respectively). The contribution from the quark transverse spin distribution h_T is suppressed by the ratio of the quark mass to the nucleon mass $\frac{m}{M}$ and should be negligible. The remaining twist-3 term reflects the quark-gluon correlations in the nucleon. This term can be obtained from the deviations from g_2^{WW}.

2 The Experiment

The E155 experiment ran in early 1997 and collected $\sim$ 180 million events. Keys to the success of E155 included the high efficiency of beam delivery, the use of lithium deuteride as the deuteron target material, and the addition of a third spectrometer. These factors enabled E155 to collect the data in 2/3 of the originally proposed time and covering almost twice the range in Q^2 as planned in the original proposal. The major components of the experiment are described below.

2.1 Polarized Electron Beam

Longitudinally polarized 48.3 GeV electron beam pulses[16] of up to 400 ns duration[17] were produced at 120 Hz by a circularly polarized laser beam illuminating a strained GaAs photocathode. The helicity for each pulse was selected by a 32-bit pseudo-random number generator to minimize instrumental asymmetries. The beam polarization P_b was determined periodically during the data run using Møller scattering from 20–154 μm thick Fe-Co-V polarized foils. Results from independent single arm[18] and coincidence detector systems agreed within 1%. No statistically significant deviations from the average value of P_b = 0.813 $\pm$ 0.020 were seen during the experiment.

2.2 Target

Fig. 3 shows a schematic of the polarized target used for E143 and E155.[19] The target material was contained in two copper-coated aluminum cups which were 3 cm long and 2.5 cm in diameter and could be moved into and out of the beam. Polarization of the material was achieved using the technique of dynamic nuclear polarization (DNP).[20] In this technique, microwaves and a high magnetic field are used to polarize paramagnetic electrons, and transfer their polarization to the nucleons. In E155, 140 GHz microwaves were delivered to each of the aluminum cups by separate waveguides. A superconducting Helmholtz pair provided a 5.004 T field with 10^{-4} uniformity in the region occupied by the material. DNP also requires the presence of paramagnetic centers (with a free or quasi-free electron). These centers were created by pre-irradiating the materials at relatively warm temperatures (80-90 K for ammonia and 180 K for lithium deuteride) and preserved by storing the material at liquid nitrogen temperatures. During normal running, a ^{4}He evaporation refrigerator kept the material at 1 K and the electron beam was rastered across the face of the target cup to minimize local polarization loss due to beam

heating. Nuclear magnetic resonance (NMR) measurements were made using coils embedded in the target materials to determine the polarization at regular intervals. These measurements were calibrated to the signal measured at thermal equilibrium (TE) near 1.6 K. These TE polarizations are small (typically $\leq 0.5\%$), but can be compared with the predictions of the Boltzmann distribution to obtain an accurate calibration.[21]

As in E143, ammonia ($^{15}NH_3$) was used as the proton target material. Polarization values of $\sim 90\%$ were typically achieved after 10 - 20 minutes. The polarization slowly decreased due to radiation damage and was restored by periodic annealing at about 80 K. Unlike E143, which used deuterated ammonia ($^{15}ND_3$), E155 used lithium deuteride[22] because it provides larger ratio of polarized (effective) deuterons to the total number of nucleons and higher radiation resistance. The lithium (^{6}Li) can, to first order, be treated as a polarized deuteron plus an unpolarized alpha particle, and therefore half of the nucleons in ^{6}LiD are the desired polarizable species.[23] Lithium deuteride is also five times as radiation resistant as $^{15}ND_3$. Pre-irradiation doses of 1.3-4.5$\times 10^{17}$e$^-$/cm^2 were used to create the paramagnetic centers necessary for dynamic nuclear polarization. An average in-beam free deuteron polarization $\langle P_t \rangle$ of 22% was achieved during E155. The maximum value was obtained after an exposure of approximately 5×10^{15}e$^-$/cm^2 in the 48.3 GeV beam (see Fig. 4). An overall relative uncertainty of 4% on P_t was achieved for the deuteron.

2.3 Spectrometers and Detectors

Scattered electrons were detected in three independent magnetic spectrometers at central angles of 2.75°, 5.5°, and 10.5° with respect to the incident beam (see Figs. 5 and 6). The spectrometers at 2.75° and 5.5° were used previously in the E154 experiment.[8] These spectrometers used two dipole magnets with opposing field directions to perform momentum selection, and the 2.75° line included a quadrupole magnet to optimize the distribution of particles at the shower counter. Electrons were identified by two threshold gas Cherenkov counters and an electromagnetic calorimeter that consisted of a 20 by 10 stack of lead glass blocks 24 radiation lengths (X_0) thick. Particle momenta and scattering angles were measured with two sets of scintillator hodoscopes. The 10.5° spectrometer was added for E155 to double the Q^2 range of the experiment (see Fig. 7). It consisted of a single dipole magnet between two quadrupole magnets followed by a scintillator hodoscope, a threshold gas Cherenkov counter, and an electromagnetic calorimeter with a preradiator (PR) section and a total absorption (TA) section. The PR

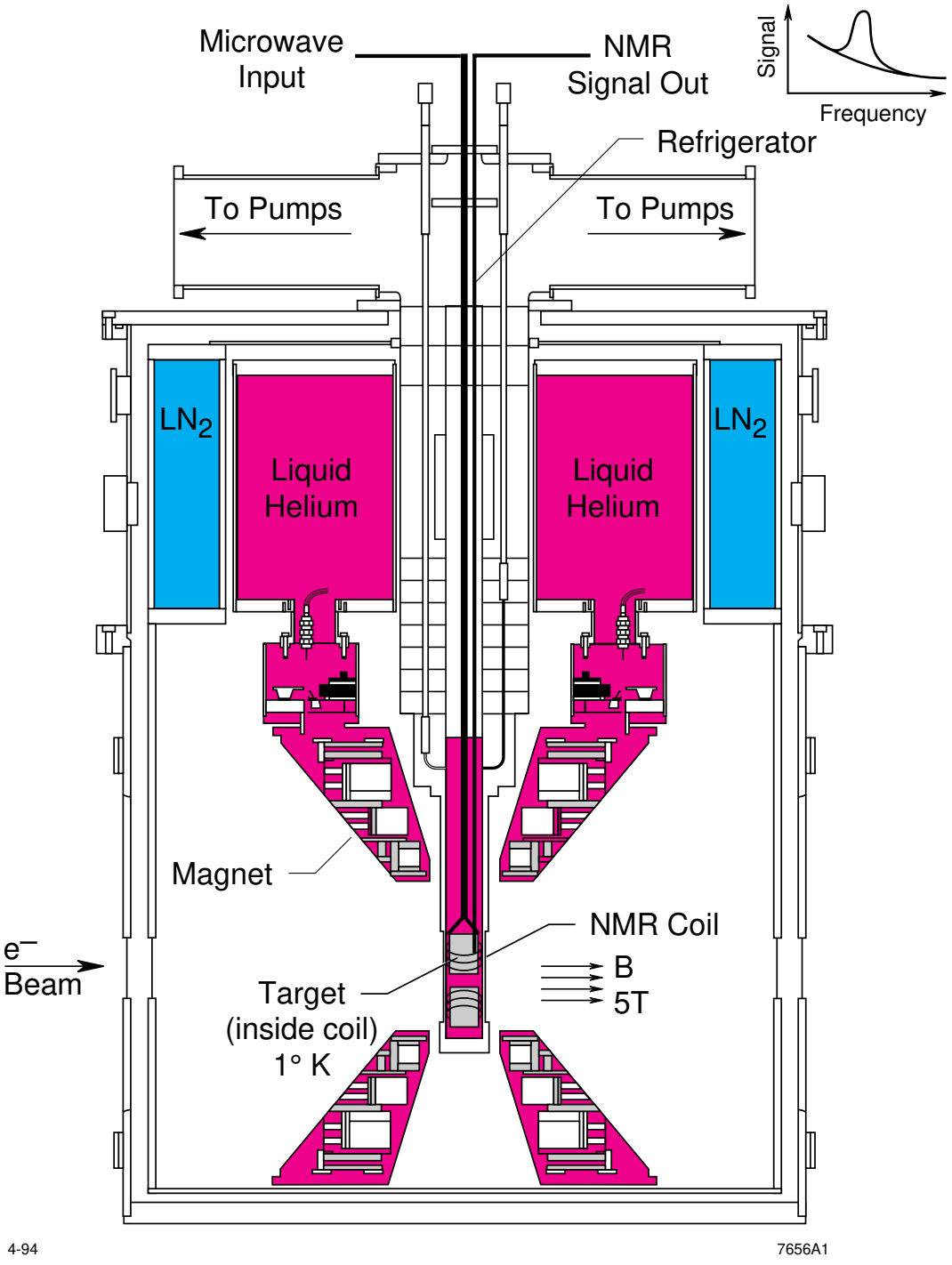

Fig. 3. The E155 target assembly

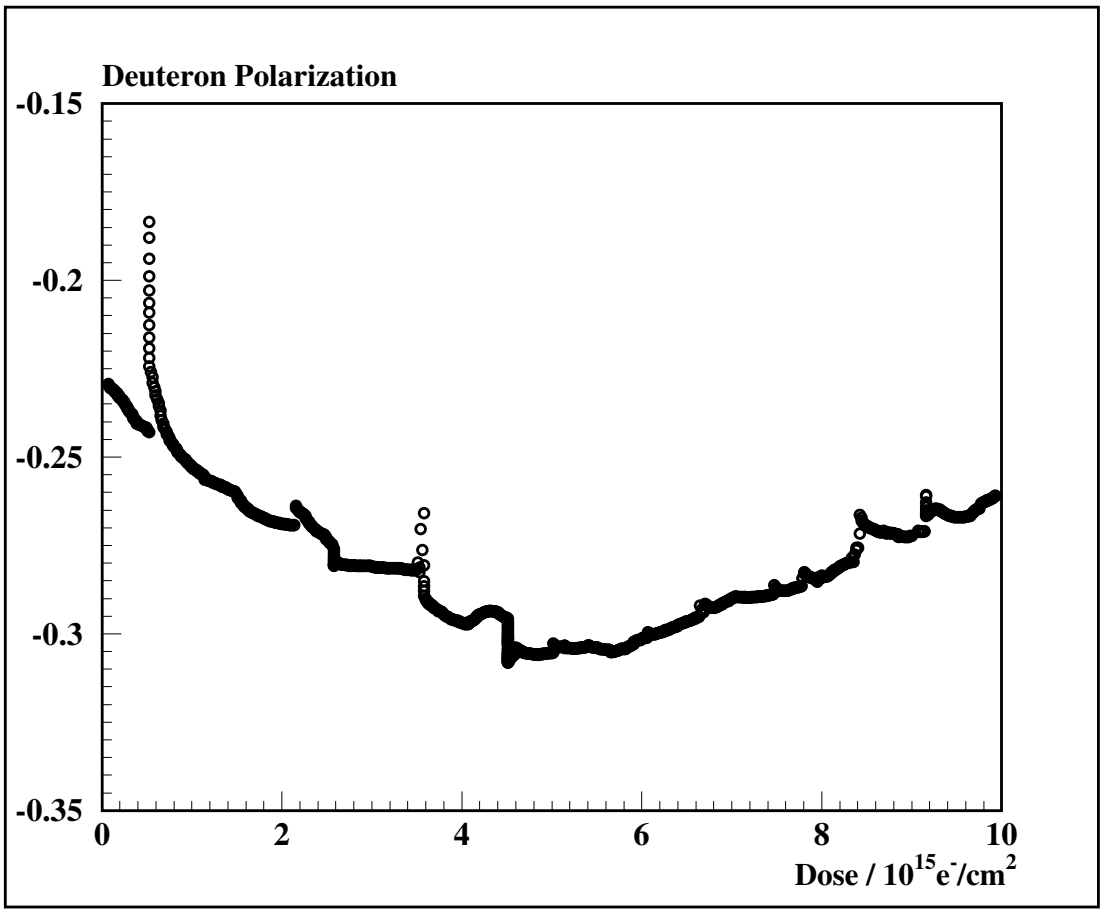

Fig. 4. Lithium Deuteride polarization as a function of accumulated dose. Deuterated ammonia shows the same behavior but reaches a maximum polarization after only 10^{15} e^{-}/cm^{2} exposure.

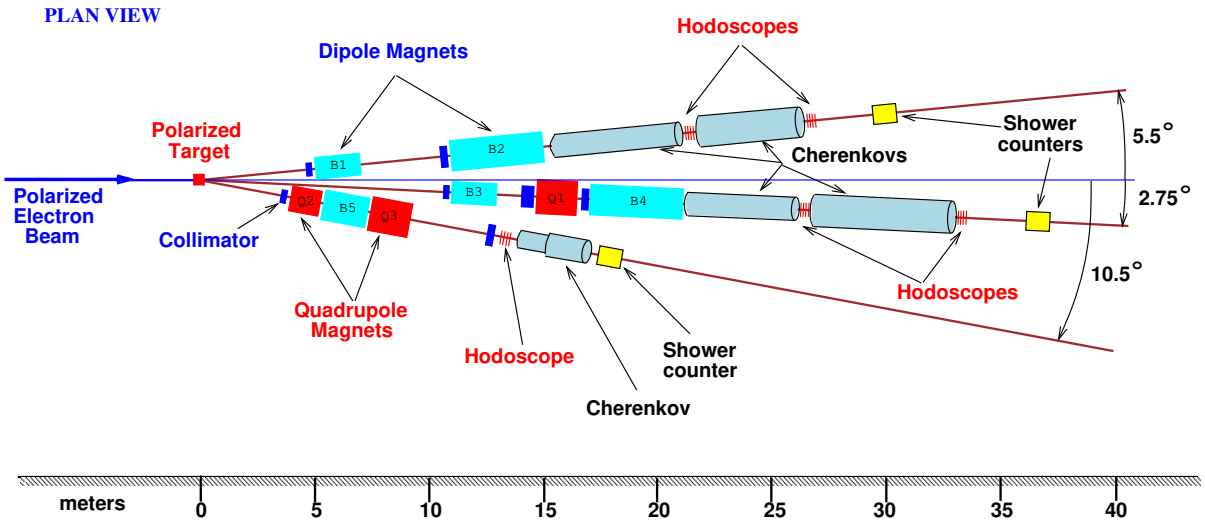

Fig. 5. Plan view of E155 spectrometers.

section consisted of ten $2X_0$ thick lead glass bars. These bars sampled the initial portion of the particle showers to separate electrons from hadrons. They were arranged to measure y position information which was combined with the hodoscope information to determine particle momenta. The TA section consisted of a 5 by 6 stack of lead glass blocks $16X_0$ thick.

3 Experimental Asymmetries

The experimental longitudinal ($A_{||}$) asymmetries were determined from the numbers of scattered electrons per incident beam charge for negative (N_-) and positive (N_+) beam helicity for each target using

$$A_{||}^d = \left(\frac{N_- - N_+}{N_- + N_+} \frac{1}{f P_b P_t C_1} - C_2 A_{||}^p \right) \frac{1}{f_{RC}} + A_{RC}. \tag{15}$$

for the deuteron and

$$A_{||}^p = \left(\frac{N_- - N_+}{N_- + N_+} \frac{1}{f P_b P_t C_1} \right) \frac{1}{f_{RC}} + A_{RC}. \tag{16}$$

for the proton. The rates N_- and N_+ were corrected for contributions from charge symmetric background processes, which were measured by reversing the spectrometer polarity. The asymmetry for the charge symmetric background is consistent with zero,

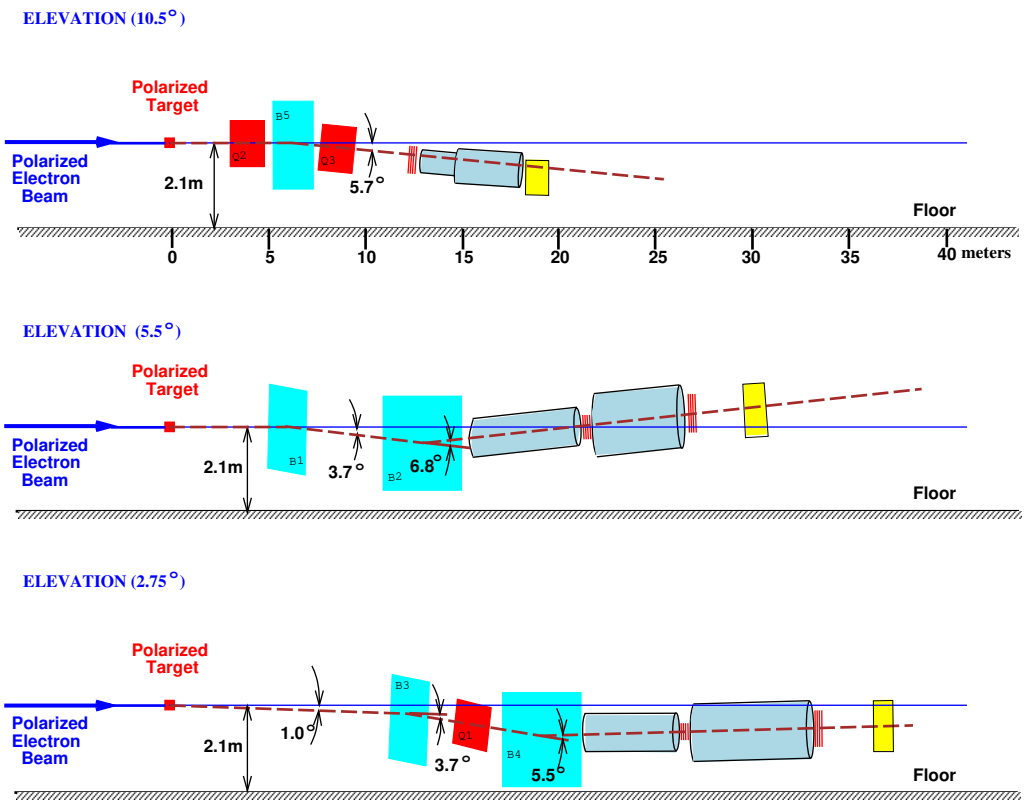

Fig. 6. Elevation view of E155 spectrometers.

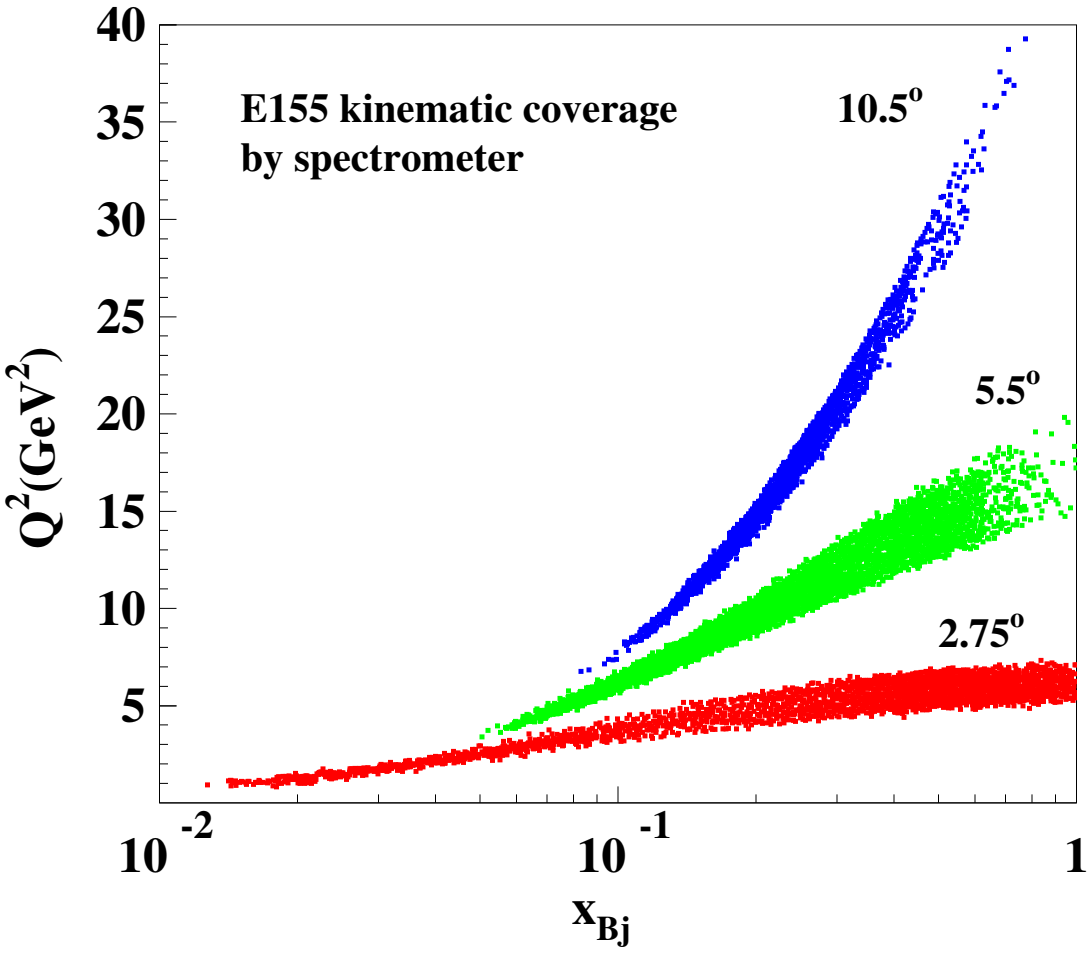

Fig. 7. x and Q^2 range for the E155 spectrometers (note the log scale for x). The data correspond to $\sim 10^6$ beam spills (a few hours of data).

leading to dilution corrections of $10\%-15\%$ at the lowest x bin in each spectrometer and decreasing rapidly at higher x. The rates N_- and N_+ were also corrected for mis-identified hadrons, which were typically about 2% or less of the electron candidates. Corrections for the rate dependence of the electron detection and reconstruction efficiency were a few percent for each spectrometer.

3.1 Dilution Factor

The dilution factor f is the fraction of events originating from the polarizable protons or free deuterons. It was determined from the composition of the target materials, containers, and NMR coils in the beam. The x dependence of the cross sections for these nuclei caused f to vary from 0.13 at low x to 0.18 at high x for the proton and from 0.18 at low x to 0.20 at high x for the deuteron. The relative systematic uncertainty on f of $\sim 2\%$ was dominated by the uncertainties of the density and packing fraction of the granules.

3.2 Nuclear Corrections

The factors C_1 and C_2 account for the presence of several polarizable nuclear species in the target. In the case of the proton, the only nuclear correction comes from the polarization of the nitrogen nuclei. This leads to a small correction of $C_1 \approx 1.015$ and no C_2 term. For the deuteron, C_1 includes the contributions from the free deuterons and effective deuterons in ^{6}Li. Calculations based on isospin conservation, shell model, solutions of Fadeev equations and a Green's function Monte Carlo provide consistent values for the valence nucleon polarization[23] in ^{6}Li. From these analyses, we conclude that the effective deuteron in ^{6}Li has a net polarization of 87% of the Li polarization. From this information we determined that C_1 ranges from 1.77 to 1.85, with an uncertainty of ± 0.05. $C_1 f$ then gives an effective dilution factor of $\sim$ 0.36 for ^{6}LiD, as compared with $\sim$ 0.22 for $^{15}ND_3$. The C_2 term accounts for contributions from polarized protons in Li^{1}H and ^{7}Li. This correction is the product of the fraction of the species present in the granules and a factor for the effective polarization of the protons. The spin-3/2 ^{7}Li nucleus is described well in terms of two clusters: an α particle and a triton. The neutrons in the triton are predominantly anti-aligned, so the only significant polarized contribution comes from the proton.[23] Values for C_2 range from -0.023 to -0.030 with an uncertainty of ± 0.003. The proton asymmetry $A_{||}^p$ was obtained from a fit to world data.

3.3 Radiative Corrections

Both internal[24] and external[25] radiative corrections were obtained using an iterative global fit of all data,[2–10] including the E155 data. Previous SLAC data were recorrected in a manner consistent with the E155 corrections. The radiative multiplicative factor f_{RC} and additive correction A_{RC} were determined in a manner similar to that used in E154.[8] This method leads to somewhat larger corrections than those in E143,[7] which only took into account the quasielastic radiative tails. For the proton, the net corrections range from 0.02 to 0.01. For the deuteron, $A_{||}$ is changed by less than 2% of its value for x above ~ 0.3, and is decreased by ~ -0.005 at low x. The x and Q^2 dependent systematic uncertainties on $A_{||}$ due to the radiative corrections were typically 0.001, 0.002, and 0.004 for the 2.75°, 5.5°, and 10.5° spectrometers, respectively.

4 Results

4.1 Longitudinal Structure Function

Preliminary results for g_1^p and g_1^d are shown in Figs. 8 and 9. A simple parameterization was used to evolve the data from the experimental values of Q^2 to $Q_0^2 = 5\ (\mathrm{GeV/c})^2$, which is roughly the average Q^2 for the experiment. The world data from proton, neutron, and deuteron targets,[2–10] including E155, with $Q^2 > 1$ (GeV/c)^2 were used to constrain separate proton and neutron functions of the form

$$(g_1/F_1) = x^\alpha(a + bx + cx^2)(1 + \beta/Q^2). \tag{17}$$

The deuteron data were included in the fit using the relation $g_1^d = \frac{1}{2}(g_1^p + g_1^n)(1 - 1.5\omega_D)$, where the deuteron D-state probability is $\omega_D = 0.05 \pm 0.01$. The variation[26] of ω_D with x is comparable to the uncertainty in ω_D for $x < 0.75$ and negligible compared to the statistical uncertainties for $x > 0.75$. The β values of -0.17 ± 0.05 and -0.14 ± 0.30 obtained from the fit are small and indicate that the Q^2 dependence of g_1 is very similar to the Q^2 dependence of the unpolarized structure function. The parameterization in Eq. 17 and F_1 determined from the recent SLAC fit for R[27] and the NMC fit for F_2[28] were used to evolve the measured g_1 data to $Q_0^2 = 5\ (\mathrm{GeV/c})^2$ as shown in Figs. 8 and 9.

The E155 results for g_1^d/F_1^d are shown in Fig. 10 as a function of Q^2. They are in good agreement with world data[2–10] as demonstrated by representative data from SMC

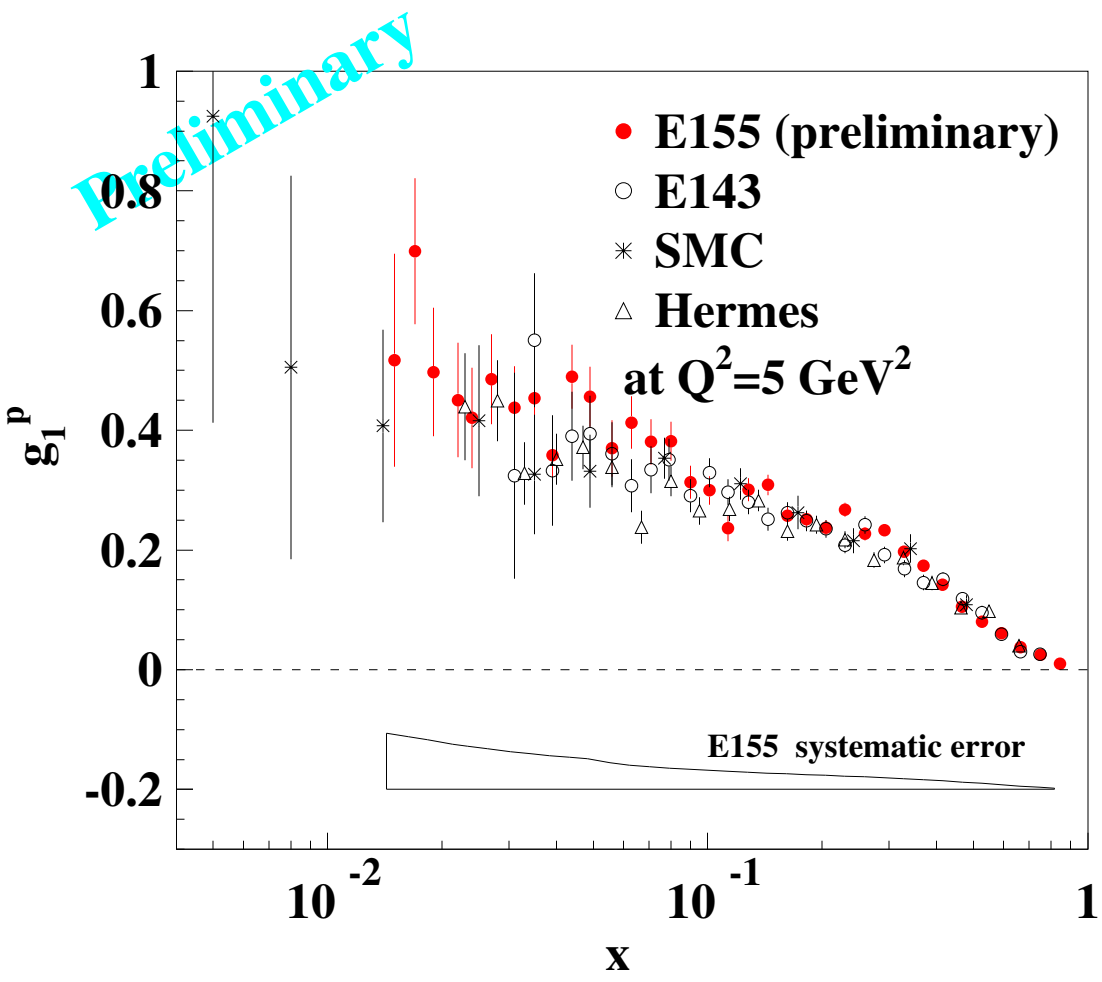

Fig. 8. Proton results for g_1^p evolved to $Q^2 = 5\ (\mathrm{GeV/c})^2$ from E155 as a function of x (filled circles). The uncertainties on the points are statistical. The shaded band indicates the systematic uncertainties. Results from E143 (open circles), SMC (stars), and HERMES (triangles) are also shown.

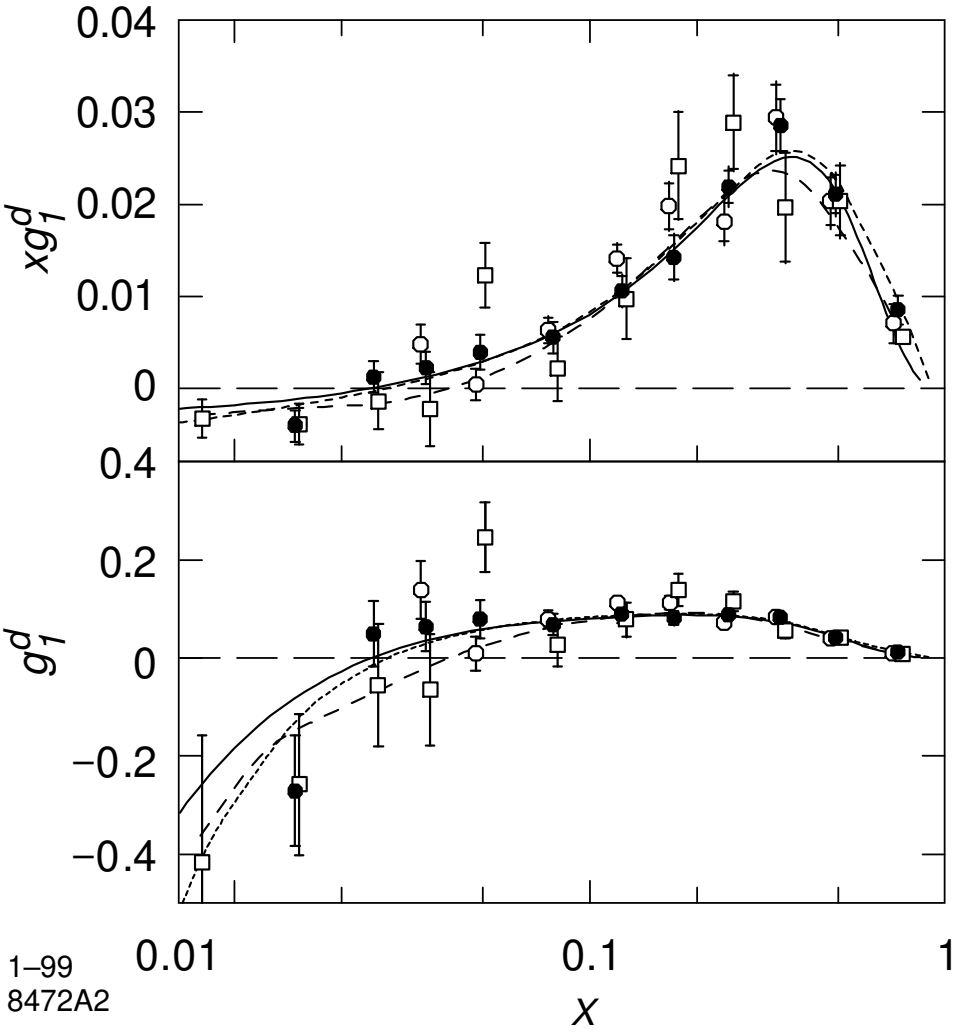

Fig. 9. Deuteron results for g_1^d (bottom) from this experiment (E155) as a function of x (filled circles). The inner bars indicate the statistical uncertainties, while the outer bars include the systematic errors in added in quadrature. The top section shows xg_1^d for E155. Results from E143 (open circles) and SMC (open boxes) are also shown.

and E143. The data from the three spectrometers provide both large Q^2 coverage and good statistical resolution in the mid-x region. There is no significant Q^2 dependence for g_1^d/F_1^d, indicating that the polarized and unpolarized structure functions evolve similarly.

Integrating g_1^d over the data range yields $\int_{0.01}^{0.9} g_1^d(x,Q_0^2)dx$ = $0.0401 \pm 0.0025(\mathrm{stat}) \pm 0.0024(\mathrm{syst})$. The extrapolation for the high x contribution was found to be negligible. However, the contribution from the low x region from 0 to 0.01 does not converge for Eq. 17, reinforcing the need for additional data at very low x. Using the E154[8] perturbative QCD fit for the low x extrapolation gives a value of $\int_0^1 g_1^d(x,Q^2)\ dx$ = $\Gamma_1^d = 0.0266 \pm 0.0025(\mathrm{stat}) \pm 0.0071(\mathrm{syst})$. Alternatively, using the SMC[11] perturbative QCD fit for the low x extrapolation gives a value of $\Gamma_1^d = 0.0291$ with comparable uncertainties.

Using the expression obtained from the operator product expansion,[7] and information on the weak hyperon decay constants from the particle data group,[29] $\Delta\Sigma$ can be extracted from Γ_1^d. Using the E154 and SMC fits for the low x region, values of $\Delta\Sigma = 0.15 \pm 0.03 \pm 0.08$ and 0.18 (respectively) are obtained in the $\overline{MS}$ scheme. These values are well below the Ellis-Jaffe prediction of 0.58,[30] but are in agreement with previous experimental values. The precision of the $\Delta\Sigma$ result obtained using only the E155 deuteron data is comparable with results obtained from NLO fits to all previous world data, such as the value of $\Delta\Sigma = 0.020 \pm 0.06 \pm 0.05$ obtained by E154.

4.2 "Transverse" Structure Function

E155 ran for a short period during the 1997 run at 38.8 GeV beam energy with the target polarization transverse to the beam direction. Results for the g_2 structure function obtained from this data are shown in Figs. 11 and 12. The data from the three spectrometers show no Q^2 dependence within the uncertainties, so the data from the spectrometers have been combined. The data correspond to a fairly short running period with the target polarization transverse to the beam, but the results are comparable with those from E143. The data are generally consistent with g_2^{WW}. However, the current results lack the power to strongly differentiate among g_2^{WW}, bag model predictions[31–33] and zero. This will be addressed by the much larger data set planned for the E155 extension run, which will focus on measurements with the target polarization perpendicular to the beam direction.

Additional information can be obtained from the moments of g_2 using the operator

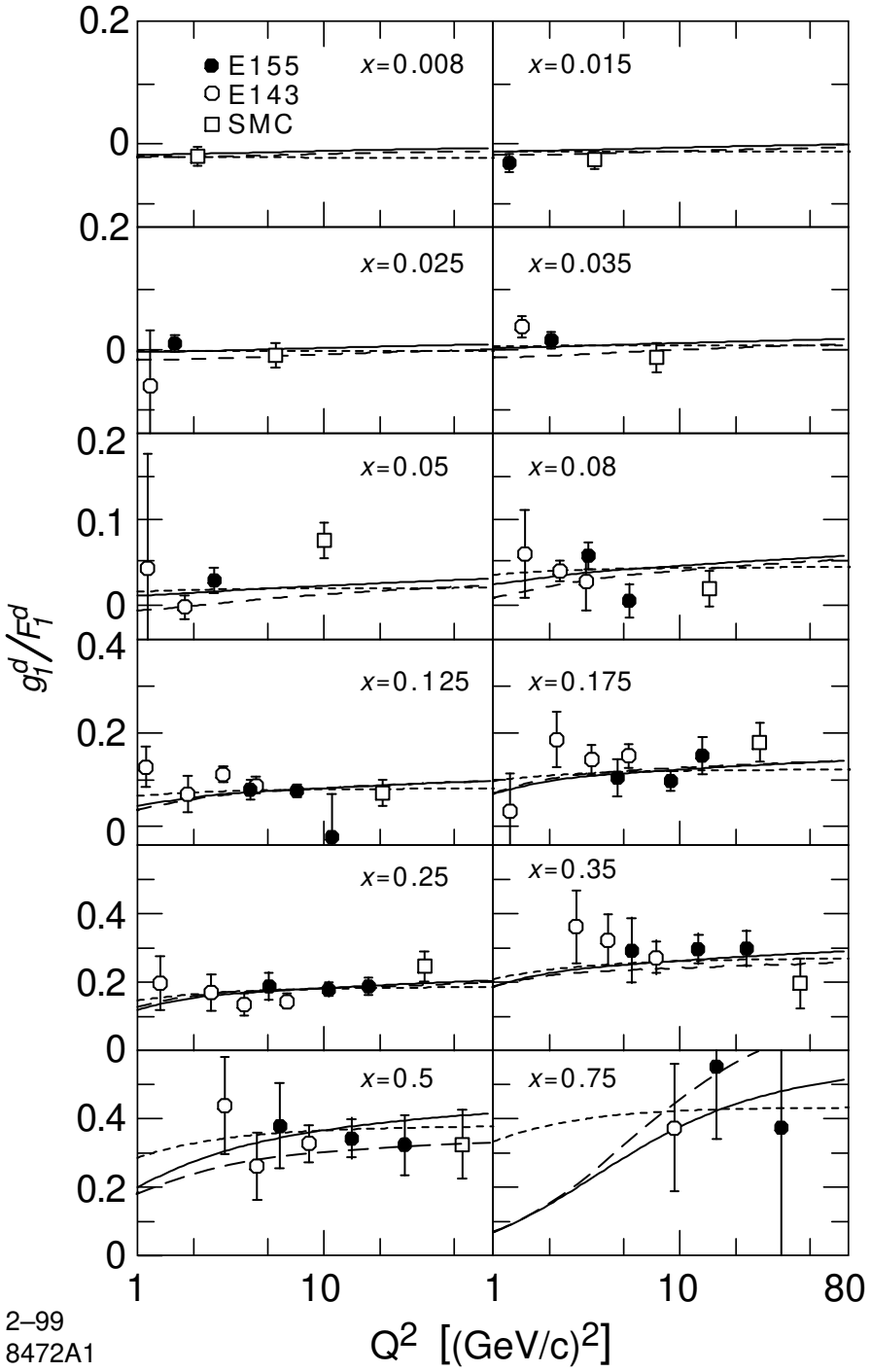

Fig. 10. Deuteron structure function ratios $\frac{g_1^d}{F_1^d}$ from E155 as a function of Q^2 for various x bins (filled circles). The inner bars indicate the statistical uncertainties, while the outer bars include the systematic errors in added in quadrature. Results from E143 (open circles) and SMC (open boxes) are also shown.

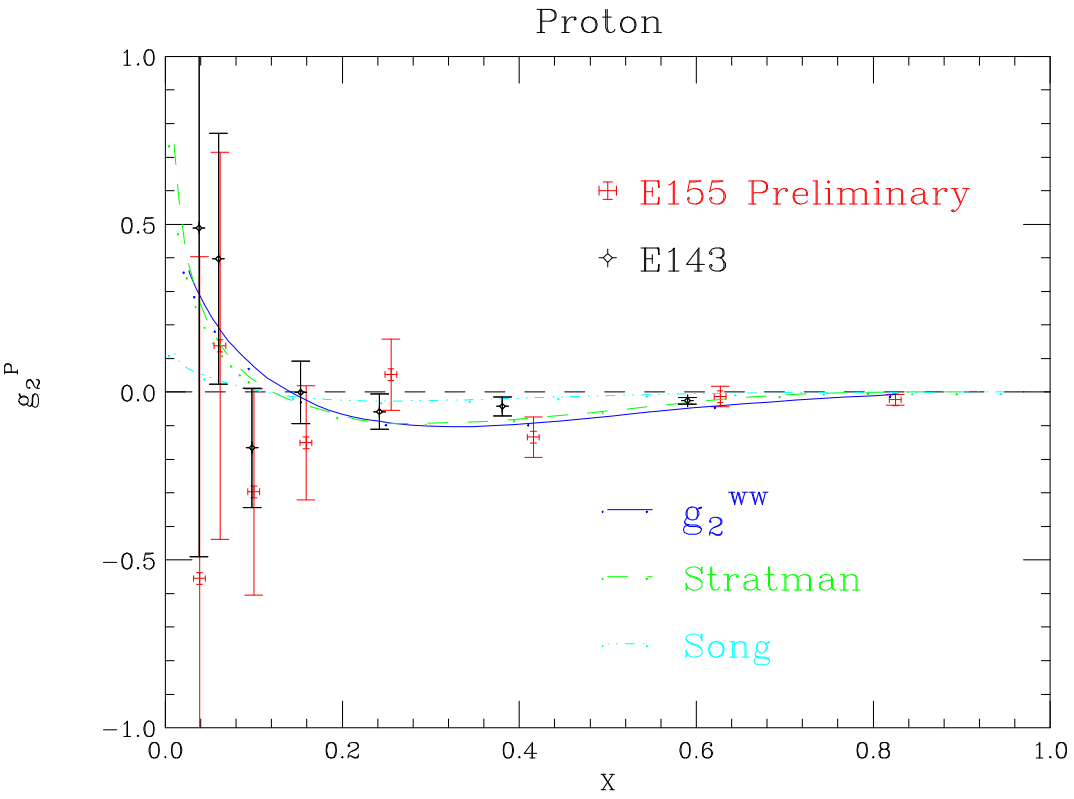

Fig. 11. Preliminary E155 results for the proton structure function g_2^p versus x (crosses). The uncertainties on the points are statistical. The E143 data have also been shown for comparison (diamonds). The solid line indicates the prediction from Wandzura and Wilczek[15] using a fit to world g_1 data. Also shown are calculations from[31] (dot-dashed line) and[32] (dashed line).

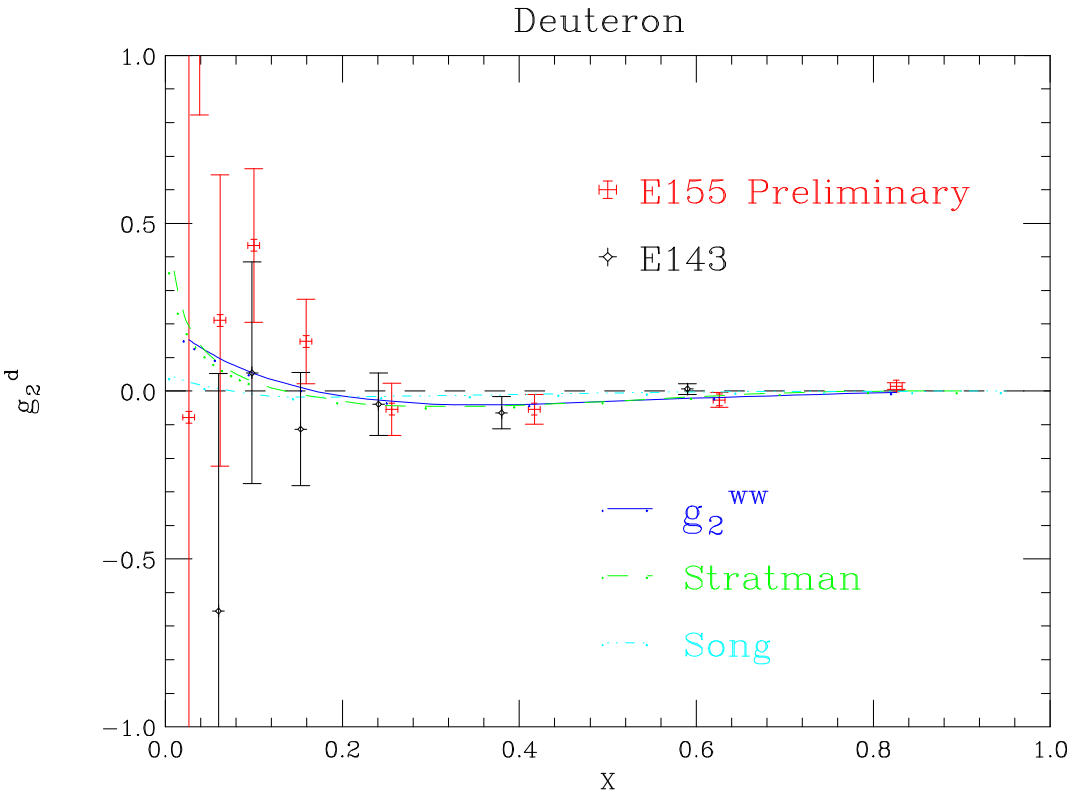

Fig. 12. Preliminary E155 results for the deuteron structure function g_2^d versus x (crosses). The uncertainties on the points are statistical. The E143 data have been also been shown for comparison (diamonds). The solid line indicates the prediction from Wandzura and Wilczek[15] using a fit to world g_1 data. Also shown are calculations from[31] (dot-dashed line) and[32] (dashed line).

product expansion (OPE). The OPE allows us to write the hadronic matrix elements in deep inelastic scattering in terms of a series of renormalized operators of increasing twist.[34,35] The moments of g_1 and g_2 at fixed Q^2 can be related to the twist-2 and twist-3 reduced matrix elements, a_n and d_n,[35] and higher twist terms which are suppressed by powers of $1/Q$. Neglecting the quark mass terms, the relations are given by

$$\Gamma_1^{(n)} = \int_0^1 x^n g_1(x,Q^2)dx = \frac{a_n}{2} + \mathcal{O}(M^2/Q^2) \quad \text{for} \quad n = 0, 2, 4, ... \tag{18}$$

$$\Gamma_2^{(n)} = \int_0^1 x^n g_2(x,Q^2)dx = \frac{1}{2}\frac{n}{n+1}(d_n - a_n) + \mathcal{O}(M^2/Q^2) \quad \text{for} \quad n = 2, 4, ... \tag{19}$$

Neglecting higher order terms and rearranging, we see that d_n measures deviations from the g_2^{WW} twist-2 prediction

$$d_n = \frac{2(n+1)}{n}\int_0^1 x^n \left[g_2(x,Q^2) - g_2^{WW}(x,Q^2)\right] dx \tag{20}$$

Evaluating this expression for $n = 2$ using the E155 data, we obtain values of $d_2^p = 0.007 \pm 0.007$ and $d_2^d = 0.008 \pm 0.005$ at an average Q^2 of 5 (GeV/c)^2. Combining these results with those from E142,[6] E143,[7] and E154[8] we obtain $d_p = 0.007 \pm 0.004$ for the proton and $d_n = 0.003 \pm 0.010$ for the neutron. Fig. 13 shows these results compared with several bag model predictions, QCD sum rule calculations, and lattice QCD. In general the results seem to be in reasonable agreement with the bag model predictions but do not favor the QCD sum rule predictions as strongly. The proton lattice QCD prediction is currently being redone. Additional data are desirable in order to differentiate between the various predictions.

5 The Future

E155 is currently completing the analysis of data taken using ammonia as the target material. When this analysis has been completed, the data from both target materials will be used along with the existing world data to perform an NLO global fit. The addition of the E155 data will improve the constraints on the parton distributions, especially the poorly understood polarized gluon distribution.

The E155 extension run, scheduled for early 1999, will be a dedicated high precision measurement of the g_2 structure function. The data from this run will significantly improve our knowledge of g_2 and will definitively distinguish between $g_2 = 0$ and g_2^{WW}. The uncertainty in d_2 will be reduced by a factor of three.

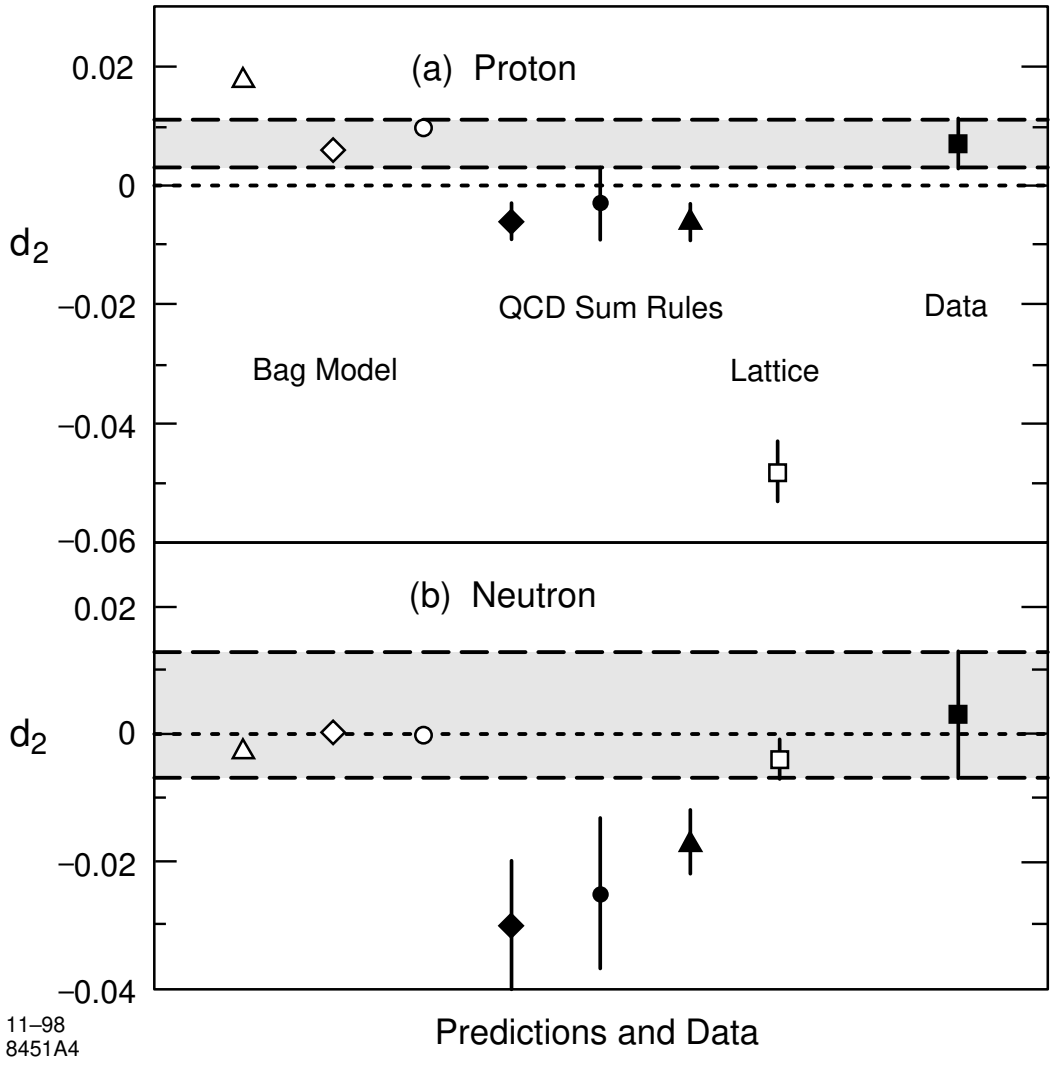

Fig. 13. SLAC results including E155 for the twist-3 element d_2. The results are in reasonable agreement with bag model calculations from Song,[31] Stratmann,[32] and Ji and Unrau.[33] The agreement with predictions from QCD sum rules from Stein *et al.*,[36] Balitsky *et al.*,[37] and Ehrnsperger *et al.*[38] is not as strong.

References

[1] R. G. Roberts, The Structure of the Proton, Cambridge Univ. Press (1990).

[2] SLAC E80, M. J. Alguard *et al.*, Phys. Rev. Lett. **37**, 1261 (1976).

[3] SLAC E130, G. Baum *et al.*, Phys. Rev. Lett. **51**, 1135 (1983).

[4] EMC, J. Ashman *et al.*, Nucl. Phys. B **328**, 1 (1989).

[5] SMC, B. Adeva *et al.*, Phys. Rev. D **58**, 112001 (1998).

[6] SLAC E142, P. L. Anthony *et al.*, Phys. Rev. D **54**, 6620 (1996);

[7] SLAC E143, K. Abe *et al.*, Phys. Rev. D **58**, 112003 (1998).

[8] SLAC E154, K. Abe *et al.*, Phys. Lett. B **405**, 180 (1997); K. Abe *et al.*, Phys. Rev. Lett. **79**, 26 (1997).

[9] SLAC E155, P. Anthony *et al.*, SLAC-Pub 7994; SLAC-Pub 8041.

[10] HERMES, A. Airapetian *et al.*, Phys. Lett. B **442**, 484 (1998); K. Ackerstaff *et al.*, Phys. Lett. B **404**, 383 (1997).

[11] SMC, B. Adeva *et al.*, Phys. Rev. D **58**, 112002 (1998).

[12] H. Georgi and H. D. Politzer, Phys. Rev. D **9**, 416 (1974); D. J. Gross and F. Wilczek, Phys. Rev. D **9**, 980 (1974).

[13] CTEQ Handbook of Perturbative QCD, Rev. Mod. Phys. **67**, Number 1, 157 (1995).

[14] G. Altarelli and G. Parisi, Nucl. Phys. B **126**, 298 (1977); V. N. Gribov and L. N. Lipatove, Sov. J. Nucl. Phys. **15**, 438, 675 (1972); Yu. L. Dokshitzer, Sov. Phys. JETP **46**, 461 (1977).

[15] S. Wandzura and F. Wilczek, Phys. Lett. B **72**, 195 (1977).

[16] R. Alley *et al.*, Nucl. Instrum. Meth. **A365**, 1 (1995); J. E. Clendenin *et al.*, Report No. SLAC-PUB-7619 (1997)

[17] F. J. Decker *et al.*, Report No. SLAC-PUB-7214 (1996)

[18] H. R. Band, G. Mitchell, R. Prepost, and T. Wright, Nucl. Instrum. Methods Phys. Res., Sect. A **400**, 24 (1997).

[19] D. G. Crabb and D. B. Day, Nucl. Instrum. Methods Phys. Res., Sect. A **356**, 9 (1995).

[20] A. Abragam, Principles of Nuclear Magnetism, Oxford University Press (1961).

[21] D. G. Crabb and W. Meyer, Annu. Rev. Nucl. Part. Sci **47**, 67 (1997).

[22] S. Bültmann *et al.*, Report No. SLAC-PUB-7904 (1998), accepted by Nucl. Instrum. Methods Phys. Res., Sect. A.

[23] O. A. Rondon, Report No. aps1998dec15_002, 1998, submitted to Phys. Rev. C.

[24] T. V. Kukhto and N. M. Shumeiko, Nucl. Phys. B **219**, 412 (1983);I. V. Akusevich and N. M. Shumeiko, J. Phys. G **20**, 513 (1994).

[25] Y. S. Tsai, Report No. SLAC-PUB-848 (1971); Y. S. Tsai, Rev. Mod. Phys. **46**, 815 (1974).

[26] W. Melnitchouk, G. Piller, and A. W. Thomas, Phys. Lett. B **346**, 165 (1995).

[27] K. Abe *et al.*, Report No. SLAC-PUB-7927, hep-ex/9808028, accepted by Physics Letters.

[28] NMC, P. Arneodo *et al.*, Phys. Lett. B **364**, 107 (1995).

[29] Particle Data Group, Eur. Phys. J. C **3**, (1998).

[30] J. Ellis and R. Jaffe, Phys. Rev. D **9**, 1444 (1974); D **10**, 1669 (1974).

[31] X. Song, Phys. Rev. D **54**, 1955 (1996).

[32] M. Stratmann, Z. Phys. C **60**, 763 (1993).

[33] X. Ji and P. Unrau, Phys. Lett B **333**, 228 (1994).

[34] E. Shuryak and A. Vainshtein, Nuc. Phys. B **201**, 141 (1982).

[35] R. Jaffe and X. Ji, Phys. Rev. D **43**, 724 (1991).

[36] E. Stein *et al.*, Phys. Lett B **343**, 369 (1995).

[37] I. Balitsky, V. Braun, and A. Kolesnichenko, Phys. Lett. B **242**, 245 (1990); B **318**, 648 (1993) (Erratum).

[38] B. Ehrnsperger and A. Schafer, Phys. Rev. D **52**, 2709 (1995).